

Cite this: *J. Mater. Chem. A*, 2015, 3, 21501

Dual-template synthesis of ordered mesoporous carbon/Fe₂O₃ nanowires: high porosity and structural stability for supercapacitors†

Junkai Hu,^a Malachi Noked,^{abd} Eleanor Gillette,^a Fudong Han,^c Zhe Gui,^a Chunsheng Wang^c and Sang Bok Lee^{*ab}

Carbon/metal oxide composites are considered promising materials for high energy density supercapacitors. So far, impregnation of the oxide into ordered mesoporous carbon materials has been demonstrated either in hard-templated carbon synthesized by using ordered mesoporous silica or alumina scaffolds, or soft-templated carbon derived from surfactant micelles. The hard-template method can provide a high pore volume but the instability of these mesostructures hinders total electrode performances upon oxide impregnation. While the soft-template methods can provide a stable mesostructure, these methods produce scaffolds with a much smaller pore volume and surface area, leading to limited metal oxide loading and electrode capacitance. Herein, anodized aluminum oxide (AAO) and triblock copolymer F127 are used together as hard and soft-templates to fabricate ordered mesoporous carbon nanowires (OMCNWs) as a host material for Fe₂O₃ nanoparticles. This dual-template strategy provides a high pore volume and surface area OMCNW that retains its stable structure even for high metal oxide loading amounts. Additionally, the unique nanowire morphology and mesoporous structure of the OMCNW/Fe₂O₃ facilitate high ionic mobility in the composite, leading to >260 F g⁻¹ specific capacitance with good rate capability and cycling stability. This work highlights the dual-template approach as a promising strategy for the fabrication of next generation heterogeneous composites for electrochemical energy storage and conversion.

Received 14th August 2015
Accepted 28th September 2015

DOI: 10.1039/c5ta06372h

www.rsc.org/MaterialsA

Introduction

Electrochemical capacitors (ECs), also called supercapacitors, have attracted great interest due to their high specific power with reasonable energy density and excellent cycling stability. In general, the ECs can be categorized into electric double layer capacitors (EDLCs) and pseudocapacitors based on their different charge-storage modes.^{1,2} The EDLCs are mainly made from carbon based materials and the energy is stored by charge

separation at the electrode/electrolyte interface;¹ while the pseudocapacitors are mostly composed of transition metal oxides or conducting polymers which store charges by fast faradaic processes involving electrochemical redox reactions.² The specific capacitance of EDLCs is limited by the total surface area of the electrode and typically not very high.³ The specific capacitance of pseudocapacitors, where redox reactions are involved, can utilize the inner part of the materials and is not limited by the surface area, hence it is anticipated to be higher than that of EDLCs.⁴ However, the most important property of supercapacitors is their high specific power, which is limited severely by the low conductivity of the metal oxides used in most of the pseudocapacitors. One strategy to obtain both specific high power and high energy is the fabrication of heterogeneous carbon/metal oxide composites for supercapacitors, as demonstrated in many previous reports.^{5–7} Among numerous carbon materials, ordered mesoporous carbons (OMCs) are good candidates as host materials for heterogeneous energy storage composites.^{8–11} This is due to their intrinsic properties, such as large electrical conductivity, high porosity, high surface area, high corrosion resistance, and easy handling. In addition, the confined metal oxide nanoparticle dimensions inside the mesopores could facilitate higher material utilization for electrochemical redox reactions.¹²

^aDepartment of Chemistry and Biochemistry, University of Maryland, College Park, MD, 20742, USA. E-mail: slee@umd.edu; Tel: +1 301 405-7906

^bDepartment of Materials Science and Engineering, University of Maryland, College Park, MD, 20742, USA

^cDepartment of Chemical and Biomolecular Engineering, University of Maryland, College Park, MD, 20742, USA

^dInstitute for Systems Research, University of Maryland, College Park, MD, 20742, USA

† Electronic supplementary information (ESI) available: The calculations of the mesopore volume difference and the specific capacitance; HRSEM images of OMCNW/Fe₂O₃; N₂ adsorption-desorption isotherms and pore size distributions of single template derived OMCs and OMC/Fe₂O₃ composites; structure comparison of FDU-15 and OMCNWs annealed at 350 °C and 900 °C; TGA curves, HRTEM images, XPS and XRD spectra of OMC/Fe₂O₃ composites; specific capacitance of OMCNW/Fe₂O₃ with different Fe₂O₃%; TEM images of OMC/Fe₂O₃ after cycling; mesopore volume changes in OMCs & OMC/Fe₂O₃ composites. See DOI: 10.1039/c5ta06372h

In general, there are two typical strategies to synthesize OMCs:¹³ the soft-template method which uses surfactant micelles as the structure directing agent;¹⁴ and the hard-template method which uses ordered porous solids, such as mesoporous silica,¹⁵ colloidal crystal,¹⁶ and anodized aluminum oxide (AAO),¹⁷ for casting a mold of the carbon replica. The soft-template method was demonstrated to preserve the desired mesoscale architecture of the host carbon material. However, due to the low surface area and pore volume of the carbon made by this method,^{18,19} the loading of oxide and the energy density are still limited.²⁰ The hard-templated carbons are reported to have a larger pore volume and surface area,²¹ which lead to higher mass loading of oxide and higher energy.^{22,23} However, the mesoporous architecture of the host carbon gradually collapses upon oxide loading, which prevented the full utilization of the inner part of the materials and limits their high rate performances.²⁰ Clearly, the soft or hard-templated OMC based composites have their own intrinsic drawbacks and merits. An ideal host OMC should have both a larger surface area and pore volume and a stable structure to achieve both high energy and power densities.

Besides the porous structure, the particle size and morphology of carbon can also influence the electrochemical performance. Xia's group²⁴ and Chen's group²⁵ have compared the electrochemical performance of ordered mesoporous carbon CMK-3 with different particle lengths and the results have shown that the shorter length results in better capacitance and rate performance due to its short pathway for rapid ion diffusion. Similarly, Chan's group^{26,27} has synthesized mesoporous hollow carbon spheres with different shell thicknesses, and found that spheres with thicker shells have hindered rate performance, due to poor ion transport. Clearly, decreasing the particle size can help to shorten the ionic transport distance and improve the electrochemical performance. However, the reduced particle size can also increase the number of solid-solid interfaces and will decrease the electronic conductivity. To overcome this, the 1D nanowire morphology is very promising due to short ion access pathways through the small nano-scale radius and efficient charge transport along its micro-scale axis.^{28–31} However, to the best of our knowledge, the structure and energy storage properties of ordered porous carbon/metal oxide nanowires have not yet been investigated.

Fe₂O₃ is low cost, non-toxic, and easy to be incorporated into a porous scaffold. It is also a promising anode material for asymmetrical supercapacitors due to its lower operating voltage window compared with other commonly used metal oxides.³² Additionally, the capacitive performance of Fe₂O₃ strongly depends on the conductivity and ion mobility,^{33,34} which made it an ideal target to study the effects of host materials on the electrochemical performance.

Using a dual-template strategy presented herein, we synthesized ordered mesoporous carbon nanowires (OMCNWs) that demonstrate the advantages of both the soft and hard-template method by achieving a high pore volume and surface area with a stable mesoporous structure. Furthermore, for the first time, we incorporated Fe₂O₃ nanoparticles into the OMCNW to fabricate OMCNW/metal oxide composites. The

dual-template strategy provides the opportunity to produce optimized structural characteristics which are not accessible using any single template. Here, the combination of the unique nanowire morphology provided by the hard-template and mesopores provided by the soft and hard-templates facilitates high Fe₂O₃ loading along with excellent ionic mobility. These structural features directly contribute to the high carbon and Fe₂O₃ capacitance, excellent rate performance and long cycle life of the OMCNWs.

Experimental

Synthesis method

Dual-templated ordered mesoporous nanowires were prepared similarly as soft-templated FDU-15,²⁰ except that an AAO membrane was used as the hard-template. In general, 0.5 g F127 was dissolved in 4.0 g ethanol. Then 3.75 g of 20% resol precursors prepared by the literature method³⁵ were added to the solution. The mixture was stirred for 1 h and then transferred to a glass Petri dish with an ethanol pre-wetted AAO, and left for 5–8 h at room temperature and 24 h at 100 °C to evaporate the ethanol. Then the gel was thermopolymerized in a 180 °C oven for 12 h, and the top resin outside of AAO was removed by using a stainless steel blade. The remaining AAO with the resin inside was scratched out and annealed in a tubular furnace at 600 °C for 3 h and subsequently at 900 °C for 2 h under Ar flow. The heating rates were 1 °C min^{−1} below 600 °C and 5 °C min^{−1} above 600 °C. The AAO membrane was dissolved using 3 M NaOH at 140 °C for 8 h in a Teflon lined autoclave, and the residual product was washed with distilled water several times.

For comparison, soft-templated FDU-15 and hard-templated CMK-8 were chosen from our previous work,²⁰ using triblock copolymer Pluronic F127 (EO₁₀₆PO₇₀EO₁₀₆, MW = 12 600) and mesoporous silica KIT-6 as the structure directing agent, respectively.

To improve the hydrophilicity of OMCs, before electrochemical testing or Fe₂O₃ loading, all three kinds of OMCs were treated with 70% HNO₃ at 60 °C for 1 h and subsequently washed with D. I. water. In order to grow Fe₂O₃ nanoparticles inside mesopores, the carbons were soaked in a 45% Fe(NO₃)₃ aqueous solution and a low pressure vacuum filtration process was used to remove any extra salt solution outside the mesopores. The mesoporous carbon with Fe(NO₃)₃ solution was heated to 100 °C for 6 h to evaporate water, followed by 190 °C annealing in argon flow for 5 h to decompose Fe(NO₃)₃ into Fe₂O₃. The final products were noted as OMCNW/Fe₂O₃, FDU-15/Fe₂O₃, and CMK-8/Fe₂O₃, where the last numbers were the weight percentages of Fe₂O₃ measured by ICP-OES.

Characterization

X-ray diffraction (XRD) patterns were recorded by using a Bruker Smart 1000 (Bruker AXS Inc., USA) using CuK α radiation. XPS analysis was done on a Kratos AXIS 165 spectrometer. The C 1s peak was calibrated at 284.8 eV. Images of mesoporous carbon and carbon/Fe₂O₃ composites were acquired using a scanning

electron microscope (Hitachi SU-70 SEM, operating at an acceleration voltage of 5 kV) and a transmission electron microscope (JEOL JEM 2100 FE-TEM, 200 kV).

Nitrogen (N_2) adsorption-desorption isotherms were recorded with a Micromeritics ASAP 2020 Porosimeter Test Station. The samples were degassed (in a vacuum) at 100 °C for 12 hours before the test. The specific surface areas were calculated using the BET method from the nitrogen adsorption branch in the relative pressure range (P/P_0) of 0.05–0.20. The porosity distribution was calculated from the adsorption branch using the BJH (Barrett-Joyner-Halenda) equation.

The loading amount of Fe_2O_3 was determined by Inductively Coupled Plasma-Atomic Emission Spectroscopy (ICP-AES) and Thermogravimetric Analysis (TGA). ICP-AES was performed on a Perkin Elmer ICP Optima 4700. Intensities were measured at 259.939 nm for Fe. Mesoporous carbon/ Fe_2O_3 samples were dissolved in a freshly prepared concentrated HCl/ethanol solution and diluted to a known volume before being administered to the plasma. The final concentration of HCl and ethanol was 2% and 0.8%, respectively. TGA was performed on a TA Instrument SDT Q600 under air flow at a rate of 20 °C min^{-1} .

Electrochemical measurements

All the electrochemical studies were performed in a standard three-electrode system utilizing a bipotentiostat (BI-STAT, Princeton Applied Research). The electrolyte was 1 M Na_2SO_3 aqueous solution. Ag/AgCl was used as the reference electrode and glassy carbon was used as the counter electrode. To make the working electrode, a slurry of the mesoporous material, carbon black, and a poly(vinylidene fluoride) (PVDF) binder at a weight ratio of 85 : 10 : 5 dispersed in *N*-methyl-2-pyrrolidone (NMP) was cast onto a stainless steel foil using a doctor blade. After drying overnight in a vacuum oven at 100 °C, the active

materials were pressed on a nickel foam current collector. The final loading amounts for the active materials were 0.5–1.0 mg cm^{-2} . The potential window was −0.8 V to 0 V vs. Ag/AgCl. Electrochemical impedance spectroscopy (EIS) was also conducted with a frequency range from 20 kHz to 10 mHz at −0.15 V vs. Ag/AgCl.

Results and discussion

Morphological and structural characterization

The structure and electrochemical performance of dual-templated OMCNW/ Fe_2O_3 were compared with those of a soft-template only FDU-15/ Fe_2O_3 , which was prepared using the same soft-template in the OMCNW but without the hard-template, AAO. The dual-templated structure was also compared to a hard-template only structure, CMK-8/ Fe_2O_3 , which has been shown previously to have the best overall performance among different mesostructured OMC/ Fe_2O_3 .²⁰

Fig. 1 presents SEM images of the three types of OMCs and OMC/ Fe_2O_3 composites. When using the soft and hard-template methods, as shown in Fig. 1a and b, carbon materials with an irregular shape were obtained. Additionally, loading of those OMCs with Fe_2O_3 does not affect the morphology (Fig. 1d and e).

The material produced using the dual-template strategy has a well-defined nanowire morphology with around 200 nm diameter and more than 10 μm length which is consistent with the original hard-template pore dimensions (Fig. 1c). This suggests the surfactant induced growth within the pores of the hard-template AAO. Furthermore, as clearly demonstrated in Fig. 1f, the morphology of the OMCNWs was maintained even after the impregnation of the oxide. No Fe_2O_3 particles can be detected outside the nanowires (Fig. S1†), indicating the

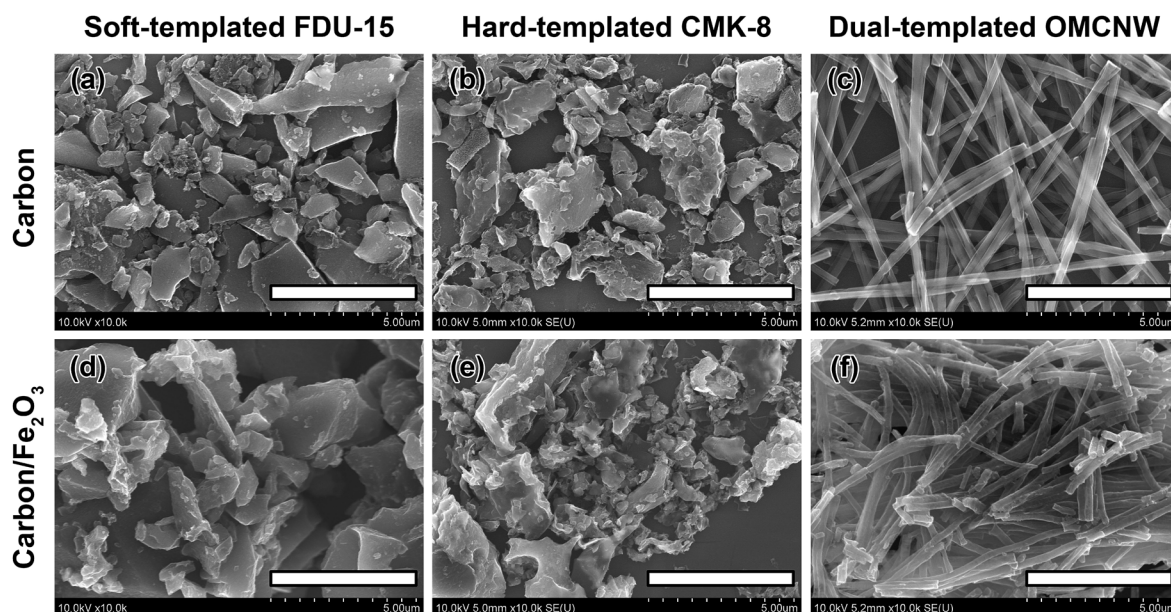


Fig. 1 SEM images of different mesostructured OMCs & OMC/ Fe_2O_3 composites: (a) FDU-15, (b) CMK-8, (c) OMCNWs, (d) FDU-15/ Fe_2O_3 , (e) CMK-8/ Fe_2O_3 , and (f) OMCNW/ Fe_2O_3 . All scale bars are 5 μm .

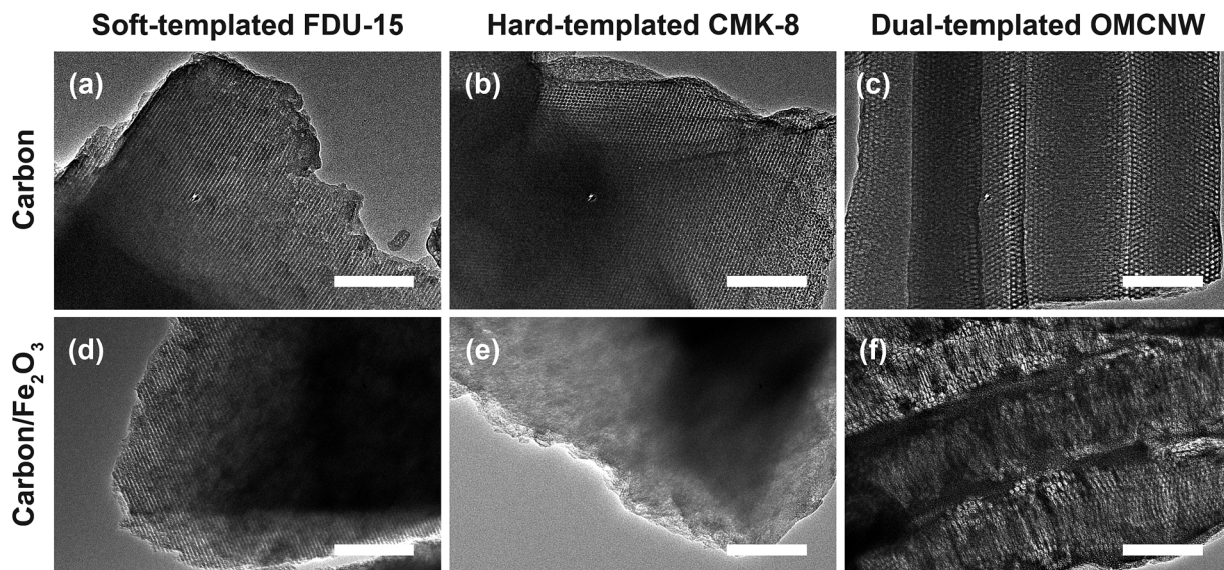


Fig. 2 TEM images of different mesostructured OMCs & OMC/Fe₂O₃ composites: (a) FDU-15, (b) CMK-8, (c) OMCNWs, (d) FDU-15/Fe₂O₃, (e) CMK-8/Fe₂O₃, and (f) OMCNW/Fe₂O₃. All scale bars are 200 nm.

selective growth of Fe₂O₃ nanoparticles inside the mesoporous system in the impregnation–decomposition processes. This is because the Fe(NO₃)₃ solution outside the mesopores was removed after filtering, in contrast, the solution inside the mesopores was preserved due to the capillary action. This different distribution of iron precursor solution would lead to the selective growth of Fe₂O₃ nanoparticles after the salt decomposition process.

The porous structures of OMCs and OMC/Fe₂O₃ composites were further characterized by using a transmission electron microscope (TEM) and N₂ adsorption–desorption isotherms. Soft-templated FDU-15 (Fig. 2a) and hard-templated CMK-8 (Fig. 2b) show a typical 1D column and 3D bicontinuous structures with pore diameters of ~4 nm. In contrast, the TEM image along the length of the OMCNW prepared using the dual-template method (Fig. 2c) shows the combined effects of both templates. The parallel arrays of straight hexagonal mesopores derived from the soft-template are reshaped to the circular

hexagonal mesopores due to the curvature of the hard-template AAO pores. In addition to the pore shape, the pore diameter is increased to ~9 nm compared with single-templated FDU-15 and CMK-8.

The N₂ adsorption–desorption isotherm of OMCNWs (Fig. 3a, open) shows the mesoporous characteristics of a type-IV curve,³⁶ which is similar to FDU-15 and CMK-3 (Fig. S2a†). A broad pore size distribution with a clear peak at the diameter of 8.7 nm is obtained for the OMCNWs (Fig. 3b, open), which is more than double the pore size in FDU-15 and CMK-3 (both are 3.8 nm, Fig. S2b†), and matches well with TEM observation. Table 1 lists the structure parameters of OMCNWs, FDU-15 and CMK-8. The total surface area and pore volume of the OMCNWs are 1063 cm² g^{−1} and 1.950 cm³ g^{−1}, which are 2 and 6 times greater than those of the soft-templated OMC (FDU-15), and are even larger than those of the hard-templated CMK-8.

Since both dual-templated OMCNWs and soft-templated FDU-15 were synthesized using the same surfactant under the

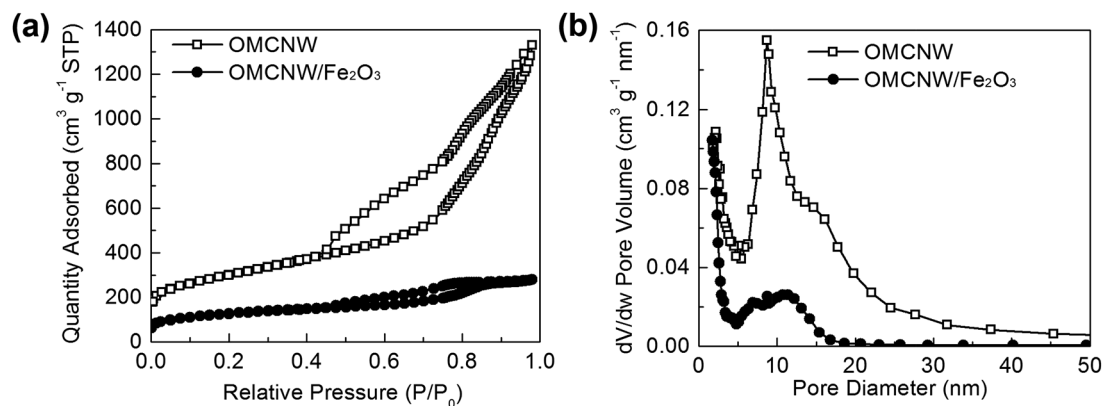


Fig. 3 N₂ adsorption–desorption isotherms (a) and pore size distributions (b) of dual-templated OMCNWs and OMCNW/Fe₂O₃ composites.

Table 1 N₂ adsorption–desorption properties of OMC composites^a

Sample ID	Soft-templated FDU-15	Hard-templated CMK-8	Dual-templated OMCNW
<i>d</i> (nm)	3.8	3.8	8.7
<i>S_t</i> (m ² g ^{−1})	554	992	1063
<i>V_t</i> (cm ³ g ^{−1})	0.327	1.178	1.950

^a All data are calculated from adsorption branches. *d*: pore diameter; *S_t* and *V_t*: total surface area and pore volume.

same conditions, we attribute the large difference in their surface area and pore volume to the AAO hard-template. In order to observe the differences in the pore structures as they evolve during the annealing process, N₂ adsorption–desorption and high-resolution TEM (HRTEM) of FDU-15 and OMCNWs annealed at 350 °C and 900 °C were used to compare the size and wall thickness of their mesopores (Fig. S3†). For FDU-15, the HRTEM images (Fig. S3c and e†) show that the mesopore wall slightly shrank from ~7 nm at 350 °C to ~6 nm at 900 °C, which is due to the volume decrease of the resin polymer during the carbonization process.³⁷ Along with this slight change in wall thickness, a ~40% decrease in the diameter of the mesopores is observed, decreasing from 6.1 nm at 350 °C to 3.8 nm at 900 °C (Fig. S3a†). The shrinkage of both the mesopore and pore wall leads to a decrease in the unit cell parameter from ~13 nm at 350 °C to ~10 nm at 900 °C, as previously reported.³⁷ OMCNWs undergo similar mesopore wall thinning (Fig. S3d and f†), however, the OMCNW pore diameter increases from 7.7 nm at 350 °C to 8.7 nm at 900 °C (Fig. S3b†), which is different from the shrinkage of the pore size in FDU-15. This difference in behavior would suggest that there is a strong interaction between the resin polymer and AAO surface since they both have a large number of hydroxyl groups.^{38–40} This interaction could help to maintain the nanowires' diameter and unit cell parameter during the carbonization process.⁴¹ Therefore, extra space is added to the mesopores in the OMCNW from the pore wall contraction. These AAO induced different structure

evolutions are illustrated in Fig. 4. Overall, the strong interactions between AAO pores and nanowires help to double the pore size and decrease the pore wall thickness, which leads to an enlarged surface area and a larger pore volume. The increase in surface area and pore volume can enhance carbon capacitance and Fe₂O₃ loading, and thus improve the electrochemical performance of OMCNW/Fe₂O₃.

ICP-OES was used to monitor the loading amount of Fe₂O₃ in 3 types of OMCs. The Fe₂O₃% of OMCNW/Fe₂O₃ (54.2%) is more than 2.5 times greater than that of the soft-templated FDU-15/Fe₂O₃ (20.0%) and even slightly higher than that of the hard-templated CMK-8/Fe₂O₃ (47.1%). Fig. S4† illustrates the thermogravimetric analysis (TGA) curves of OMC/Fe₂O₃, which show similar Fe₂O₃% to the ICP-OES. For both characterization methods, the Fe₂O₃% follows the same trend of FDU-15/Fe₂O₃ < CMK-8/Fe₂O₃ < OMCNW/Fe₂O₃. The high mass loading of OMCNW/Fe₂O₃ is attributed to the optimized porous structure and pore volume enabled by dual-template methodology.

Although OMCNW/Fe₂O₃ has even higher Fe₂O₃% loading than hard-templated CMK-8/Fe₂O₃, it does not suffer mesostructure collapse upon Fe₂O₃ loading. In Fig. 3, OMCNW/Fe₂O₃ still shows a type-IV mesoporous characteristic adsorption–desorption curve, with a broad mesopore size distribution range (5–16 nm) which is similar to the OMCNW, indicating a maintained mesostructure. Similarly, in Fig. S2b,† the pore size of FDU-15/Fe₂O₃ is 3.8 nm, which is same as that of FDU-15. In contrast, the pore size decreased from 3.8 nm in CMK-8 to less than 1.7 nm in CMK-8/Fe₂O₃, indicating a complete loss of mesoporosity.

The mesostructural change upon Fe₂O₃ loading is further evaluated by the mesopore volume difference between OMC/Fe₂O₃ composites and their corresponding OMCs (ΔV_{meso} %, see ESI† for detailed calculations). Due to the occupation of Fe₂O₃, the mesopore volume in the OMC/Fe₂O₃ composite is smaller than that in the original OMC, and the mesopore volume change should be proportional with the Fe₂O₃ loading amount. As shown in Table S1,† the ΔV_{meso} % of dual-templated OMCNW/Fe₂O₃ (59.0%) and soft-templated FDU-15/Fe₂O₃ (20.7%) is similar to their Fe₂O₃ loading amount (54.2% for

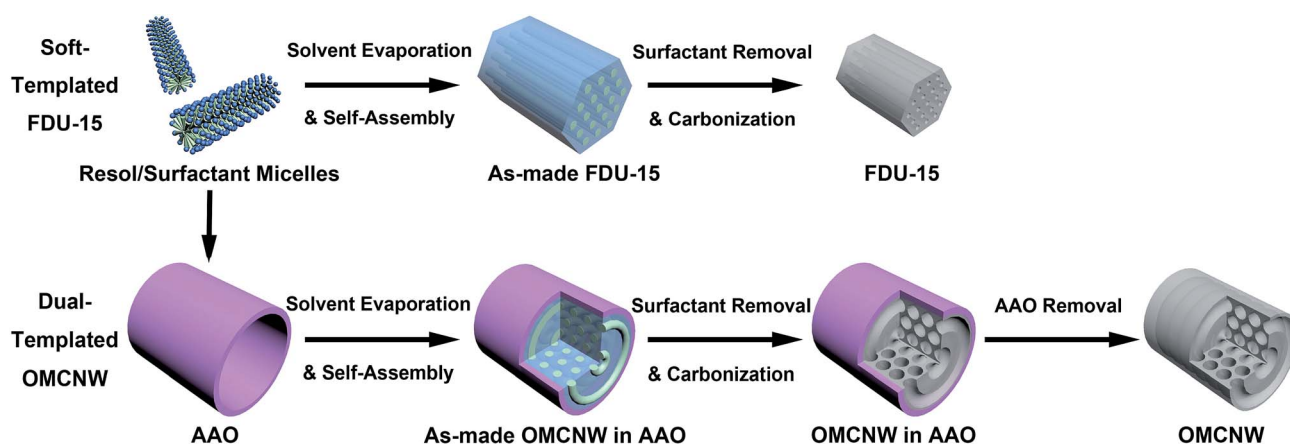


Fig. 4 Schematic illustration of different mesostructure evolutions of mesoporous carbon synthesized with & without AAO.

OMCNW/Fe₂O₃, and 20.0% for FDU-15/Fe₂O₃). In contrast, the $\Delta V_{\text{meso}}\%$ of hard-templated CMK-8/Fe₂O₃ (80.5%) is much higher than its Fe₂O₃% (47.1%). This extra mesopore volume loss indicates a structure collapse in the CMK-8/Fe₂O₃. Therefore, we can clearly conclude that the structural stability of the dual-templated OMCNW is similar to the soft-templated FDU-15, and is much more stable than the hard-templated CMK-8. This is also supported by TEM images: Fig. 2d and S5a† show the well-preserved 1D column mesopores in FDU-15/Fe₂O₃, while Fig. 2f and S5c† present the circular mesostructure in OMCNW/Fe₂O₃. In contrast, as shown in Fig. 2e and S5b,† the ordered 3D mesostructure has completely disappeared in CMK-8/Fe₂O₃. The unstable mesopores of CMK-8 are due to the fragility of structure-supporting nano-bridges derived from the micropores (<2 nm)⁴² in the original silica template. In the Fe₂O₃ growth process, the released gasses (H₂O and NO_x) or the volume change during the Fe(NO₃)₃ to Fe₂O₃ transformation could easily break the nano-bridges and thus the mesoporous architecture.²⁰ In the case of OMCNWs and FDU-15, both of which include the surfactant as the mesostructure directing agent, rigid carbon networks are formed around the tubular surfactant micelles (Fig. 4).³⁵ Therefore, their structure is more tolerant toward solvent evaporation or salt decomposition in the Fe₂O₃ growth process. It is worth noting that, owing to the extremely high mesopore volume of OMCNWs, even after loading of Fe₂O₃, the OMCNW/Fe₂O₃ still has 0.322 cm³ g⁻¹ mesopore volume, which is higher than that of the other two OMC/Fe₂O₃ composites derived from single-templated carbons. The large reserve of mesopores is anticipated to act as fast ion pathways which will improve ion mobility and accessibility during electrochemical processes.

The valence state of iron oxide in the OMCNW/Fe₂O₃ composite was determined by X-ray photoelectron spectroscopy (XPS) (Fig. S6a†). Three broad peaks at 711 eV, 719 eV, and 724 eV are in agreement with the reported value for Fe₂O₃,⁴³ which is the same as that for single-templated FDU-15/Fe₂O₃ and CMK-8/Fe₂O₃ derived by similar Fe₂O₃ incorporation steps. The X-ray diffraction (XRD) patterns of OMC/Fe₂O₃ composites (Fig. S6b†) have no distinguished peaks, indicating the poor crystallinity of Fe₂O₃ nanoparticles due to a low annealing temperature of 190 °C.

Electrochemical studies

The cyclic voltammetry (CV) curves were used to evaluate the capacitance performance of different samples in 1 M Na₂SO₃ aqueous solutions. The Na₂SO₃ solution is a commonly used electrolyte for Fe₂O₃ materials^{40,33,44–49} because of the extra capacitance gained from the redox reaction of SO₃²⁻.^{45,49} The CV responses of the 3 types of OMCs at a scan rate of 5 mV s⁻¹ are presented in Fig. 5a. All of the curves have a rectangular shape, which is a characteristic of electrochemical double layer capacitance (EDLC). The specific capacitance of the OMCNW, CMK-8, and FDU-15 is 145 F g⁻¹, 113 F g⁻¹, and 87 F g⁻¹, respectively, which is a similar trend to the surface area values of the OMCs. The capacitances of different OMCs at various scan rates are presented in Fig. 5c, which clearly demonstrated the highest capacitances in the OMCNW for all scan rates.

The CV curves of OMC/Fe₂O₃ composites are shown in Fig. 5b. For all of the OMC/Fe₂O₃ composites, especially for OMCNW/Fe₂O₃ and CMK-8/Fe₂O₃ which have a high Fe₂O₃ content, the peaks at ~-0.3 V and <-0.6 V are typical for redox reactions from sulfite anions adsorbed on Fe₂O₃ and redox reactions between Fe(II) and Fe(III).^{33,45} The larger areas of CV curves in OMC/Fe₂O₃ composites indicate increased capacitance upon Fe₂O₃ loading.

The capacitance of the different mesostructured OMC/Fe₂O₃ composites at scan rates between 5 mV and 200 mV is shown in Fig. 5d. Regardless of the scan rate, the OMCNW/Fe₂O₃ exhibits the highest specific capacitance among all three OMC/Fe₂O₃ composites.

As the OMC/Fe₂O₃ composites were made using OMCs and iron oxide, there are three factors which determine the value of the composite capacitance (C_{total}): the carbon capacitance (C_{C}), the iron oxide capacitance ($C_{\text{Fe}_2\text{O}_3}$), and the loading amount of Fe₂O₃ (Fe₂O₃%). Here, these three factors in different mesostructures are compared to evaluate the structural effects on electrochemical performance.

As discussed above, due to the high surface area, C_{C} of dual-templated OMCNWs is much higher than that of single-templated FDU-15 and CMK-8, which provides a good starting point to achieve a high capacitance of the OMCNW/Fe₂O₃.

In order to compare the Fe₂O₃ capacitance, $C_{\text{Fe}_2\text{O}_3}$ was calculated using the following equation based on the Fe₂O₃% and capacitance difference of OMCs and OMC/Fe₂O₃:

$$C_{\text{Fe}_2\text{O}_3} = \frac{C_{\text{total}} - C_{\text{C}} \times (1 - \text{Fe}_2\text{O}_3\%)}{\text{Fe}_2\text{O}_3\%}$$

The calculated Fe₂O₃ capacitances are shown in Fig. 5e. The hard-template derived CMK-8/Fe₂O₃, especially for high scan rates, demonstrated the lowest Fe₂O₃ capacitance due to the limited ion transport in the collapsed mesopores. On the other hand, for soft-template derived FDU-15/Fe₂O₃, due to the small Fe₂O₃% and favorable ion transportation in the well preserved mesopores, the Fe₂O₃ capacitance is higher than the other two OMC/Fe₂O₃ for all scan rates. In the case of dual-template derived OMCNW/Fe₂O₃, the well preserved mesostructure and small nanowire diameter lead to a good ionic transportation, which results in higher $C_{\text{Fe}_2\text{O}_3}$ than CMK-8/Fe₂O₃. However, due to the higher Fe₂O₃% and larger pore diameter in OMCNW/Fe₂O₃, its Fe₂O₃ nanoparticle size is larger than that in FDU-15/Fe₂O₃, which decreases the utilization of Fe₂O₃ and results in a smaller $C_{\text{Fe}_2\text{O}_3}$ in OMCNW/Fe₂O₃ than that in FDU-15/Fe₂O₃.

Although the Fe₂O₃ capacitance in OMCNW/Fe₂O₃ is slightly smaller than that in FDU-15/Fe₂O₃, the OMCNW/Fe₂O₃ has the highest Fe₂O₃% of 54.2%, which is about two times higher than FDU-15/Fe₂O₃ (20.0%). As shown in Fig. S7,† the specific composite capacitance is increased with the increase of Fe₂O₃ content. This is due to the much higher capacitance of Fe₂O₃ than that of carbon. Therefore, OMCNW/Fe₂O₃ with higher Fe₂O₃% can gain much more capacitance improvement from the Fe₂O₃ contribution.

Overall, the balanced structural properties in the dual-templated OMCNW/Fe₂O₃ ensure the highest carbon capacitance & Fe₂O₃ loading amount and a moderate iron oxide capacitance,

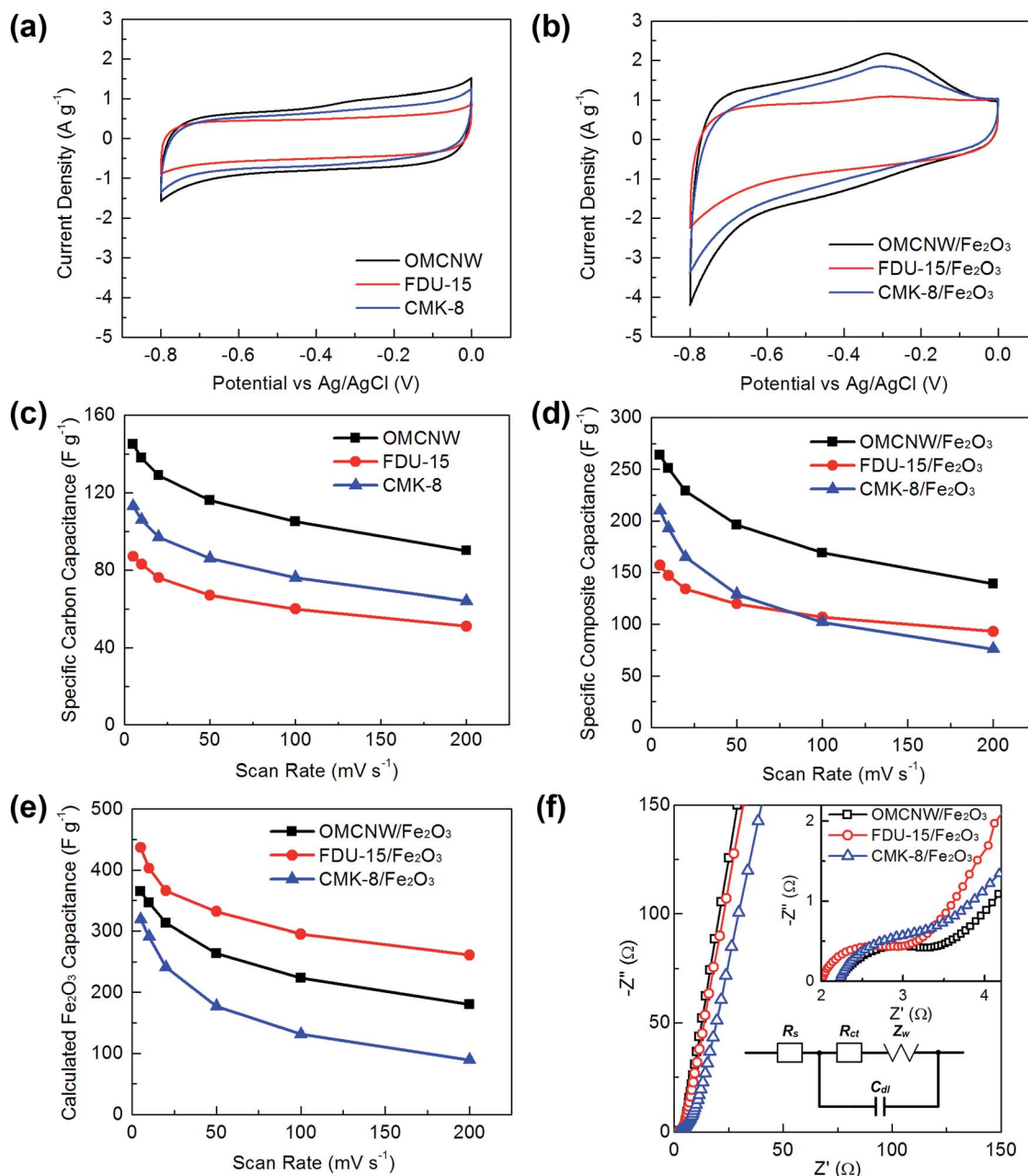


Fig. 5 Cyclic voltammetry curves of OMCs (a) and OMC/Fe₂O₃ composites (b) in 1 M Na₂SO₃ at a scan rate of 5 mV s⁻¹. (c & d) Specific capacitances of OMCs (c) and OMC/Fe₂O₃ composites (d) at different scan rates. (e) Calculated Fe₂O₃ capacitances of different OMC/Fe₂O₃ composites at different scan rates. (f) Nyquist plots of OMC/Fe₂O₃ composites, bottom inset: equivalent Randles circuit.

which lead to 264 F g⁻¹ total capacitance of OMCNW/Fe₂O₃ at 5 mV s⁻¹. This capacitance value is much higher than that of the FDU-15-20 (157 F g⁻¹) and CMK-3-47.2 (210 F g⁻¹). In addition,

Table 2 EIS parameters of different OMC/Fe₂O₃ composites

Sample ID	Soft-templated FDU-15/Fe ₂ O ₃	Hard-templated CMK-8/Fe ₂ O ₃	Dual-templated OMCNW/Fe ₂ O ₃
R_s (Ω)	2.0	2.2	2.2
R_{ct} (Ω)	1.1	1.3	1.3
Z_w (Ω)	2.1	6.8	0.8

due to the good electronic conductivity along the nanowires and favorable ionic mobility through the well preserved mesopores in the ~100 nm nanowire radius, the OMCNW/Fe₂O₃ exhibits an excellent rate performance, with a specific capacitance of 139 F g⁻¹ at 200 mV s⁻¹.

The good ion mobility in OMCNW/Fe₂O₃ can be observed by electrochemical impedance spectroscopy (EIS). As shown in Fig. 5f, all Nyquist plots of OMC/Fe₂O₃ composites are similar in shape with an arc at high frequencies, followed by a straight line inclined at around 45° to the real axis in the medium frequencies, and a nearly vertical line in the low frequency region. Such

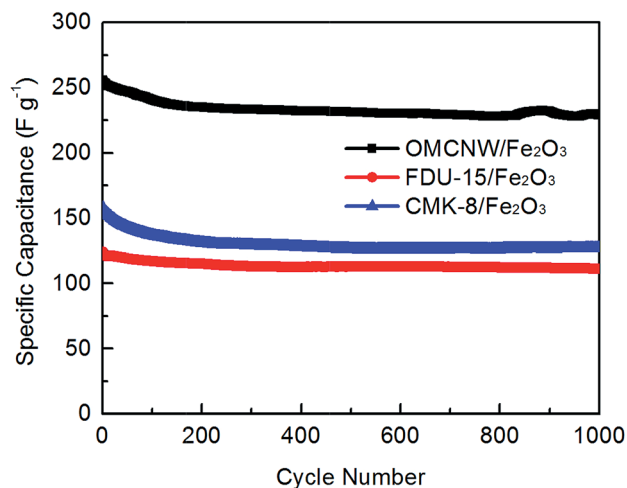


Fig. 6 Cycling performance of different OMC/Fe₂O₃ composites.

a Nyquist plot pattern is typical of an equivalent Randles circuit (bottom inset of Fig. 5f).^{32,34,50–55}

Table 2 lists the values of each circuit component for the different composites. For all samples, the solution resistance (R_s) is similar (2.0–2.2 Ω). Due to the larger Fe₂O₃ particle size in OMCNW/Fe₂O₃ and CMK-8/Fe₂O₃, the charge transfer resistance (R_{ct}) of them (1.3 Ω) are slightly larger than that in FDU-15/Fe₂O₃ (1.1 Ω). The impedance of ion transportation in the porous system can be simulated by the transmission line model, which is constituted by a large network of resistors and capacitors.⁵⁶ Since the mathematical model and impedance formula of the transmission line are equivalent with the Warburg impedance (Z_w),^{57–59} here, we use Warburg impedance to reflect the ion transport process in the porous electrode. As listed in Table 2, Z_w of OMCNW/Fe₂O₃, FDU-15/Fe₂O₃ and CMK-8/Fe₂O₃ are 0.8 Ω , 2.1 Ω , and 6.8 Ω , respectively. The small Z_w of OMCNW/Fe₂O₃ not only attributed to the good ion transportation in the well preserved mesopores, but also to the enhanced ion mobility from the small radius in the nanowire morphology.

Finally, we evaluated the capacitance retention upon cycling of OMC/Fe₂O₃ composites by a galvanostatic charge–discharge test at a current density of 5 A g^{−1}. The specific capacitances as a function of the cycle number are compared in Fig. 6. After 1000 cycles, the OMCNW/Fe₂O₃ still has a capacitance of 229 F g^{−1}, which shows a good capacitance retention of 89.5%. This capacitance retention is similar to FDU-15/Fe₂O₃ (89.8%), and attributed to the good structural stability, which is supported by the well preserved ordered structures under TEM after 1000 cycles (Fig. S8†). In contrast, lower capacitance retention (80.4%) was found in CMK-8-47.2, indicating a less stable capacitance in the fragile hard-template derived carbon framework.

The comparison of the structural properties and electrochemical performance between the three types of OMCs used herein are presented in Table 3. Clearly, the dual-templated OMCNW presents the structural advantages of both soft and hard-templated OMCs and avoids their drawbacks, which leads to the best electrochemical performance of OMCNW/Fe₂O₃.

Conclusions

A dual-template strategy was used to synthesize ordered mesoporous carbon nanowires by conjugating soft-template and hard-template methodologies and was applied, for the 1st time, as an oxide host material to form OMCNW/Fe₂O₃ composites. The structural properties and electrochemical performance of dual-templated OMCNW/Fe₂O₃ were compared with soft- and hard-templated OMCs/Fe₂O₃ composites. The OMCNW from the dual-template strategy has double the total surface area, and six times the total pore volume when compared to the soft-templated FDU-15. Compared with hard-template synthesized CMK-8, the OMCNW still presents good mesostructural stability and ion mobility. In addition, the morphology of the hard-template was well maintained as the synthesized 1D nanowires were a few microns in length and ~100 nm in radius. All of these structural properties made the OMCNW an ideal scaffold for heterogeneous host materials for high performance

Table 3 Structural properties and electrochemical performance comparison of OMCs from different synthetic strategies as host materials of Fe₂O₃

Preparation method	Soft-template (FDU-15)	Hard-template (CMK-8)	Dual-template (OMCNW)
Structural properties			
Surface area (m ² g ^{−1})	Small (554)	Large (992)	Large (1063)
Pore volume (m ³ g ^{−1})	Small (0.327)	Large (1.178)	Large (1.950)
Pore size (nm)	Small (3.8)	Small (3.8)	Large (8.7)
Structural stability (from TEM)	Stable	Unstable	Stable
Morphology	Micron sized particles	Micron sized particles	Nanowires
Electrochemical performances			
Carbon capacitance (F g ^{−1} at 5 mV s ^{−1})	Small (87)	Medium (113)	Large (145)
Fe ₂ O ₃ capacitance (F g ^{−1} at 5 mV s ^{−1})	Large (437)	Small (319)	Medium (365)
Fe ₂ O ₃ loading amount (%)	Low (20.0)	High (47.1)	High (54.2)
OMC/Fe ₂ O ₃ capacitance (F g ^{−1} at 5 mV s ^{−1})	Small (157)	Medium (210)	Large (264)
Ion accessibility (evaluated by Z_w , Ω)	Easy (2.1)	Hard (6.8)	Easy (0.8)
High rate capacitance retention (C_{200}/C_5 , %)	Large (59)	Small (36)	Large (53)
Cycling stability (% after 1000 cycles)	Stable (89.8)	Moderate (80.4)	Stable (89.5)

supercapacitors. The large surface area leads to a high carbon capacitance contribution, while the large pore volume and the stable carbon scaffold provide high Fe_2O_3 loading of over 50% without the mesostructure degradation. Additionally, the nanowires with a micro-sized length could form a network to improve electronic conductivity, while the small radius of nanowires together with a larger mesopore volume help to enhance the ionic mobility and accessibility, and ensure a high Fe_2O_3 capacitance. Overall, the OMCNW/ Fe_2O_3 composite was able to deliver the highest specific capacitance of 264 F g^{-1} at 5 mV s^{-1} , with good rate capability and cycling performance. The synergistic effects of the dual-template method demonstrated in this work have a significant impact on design of electrode materials on both the mesoscale porous structure and macroscale morphology and could be applied in other electrochemical energy storage systems to improve both energy density and power density.

Acknowledgements

The work was supported by the Nanostructures for Electrical Energy Storage (NEES), an Energy Frontier Research Centre funded by the US Department of Energy, Office of Science, Office of Basic Energy Sciences under Award Number DESC0001160. We thank Sz-Chian Liou, and Wen-An Chiou (AIM lab) for their assistance with the SEM and TEM imaging. We thank Lu Liu and Michael Zachariah for their assistance with the TGA. Finally; we thank Karen Gaskell for her help with the XPS results.

Notes and references

- 1 L. L. Zhang and X. S. Zhao, *Chem. Soc. Rev.*, 2009, **38**, 2520–2531.
- 2 G. P. Wang, L. Zhang and J. J. Zhang, *Chem. Soc. Rev.*, 2012, **41**, 797–828.
- 3 Y. W. Zhu, S. Murali, M. D. Stoller, K. J. Ganesh, W. W. Cai, P. J. Ferreira, A. Pirkle, R. M. Wallace, K. A. Cychoz, M. Thommes, D. Su, E. A. Stach and R. S. Ruoff, *Science*, 2011, **332**, 1537–1541.
- 4 Z. Yang, J. Ren, Z. Zhang, X. Chen, G. Guan, L. Qin, Y. Zhang and H. Peng, *Chem. Rev.*, 2015, **115**, 5159–5223.
- 5 R. Liu, J. Duay and S. B. Lee, *Chem. Commun.*, 2011, **47**, 1384–1404.
- 6 J. W. Lee, A. S. Hall, J.-D. Kim and T. E. Mallouk, *Chem. Mater.*, 2012, **24**, 1158–1164.
- 7 Z. Chen, V. Augustyn, J. Wen, Y. W. Zhang, M. Q. Shen, B. Dunn and Y. F. Lu, *Adv. Mater.*, 2011, **23**, 791–795.
- 8 H. Jiang, J. Ma and C. Z. Li, *Adv. Mater.*, 2012, **24**, 4197–4202.
- 9 E. Lim, H. Kim, C. Jo, J. Chun, K. Ku, S. Kim, H. I. Lee, I. S. Nam, S. Yoon, K. Kang and J. Lee, *ACS Nano*, 2014, **8**, 8968–8978.
- 10 Y. Lin, X. Y. Wang, G. Qian and J. J. Watkins, *Chem. Mater.*, 2014, **26**, 2128–2137.
- 11 K. Pinkert, L. Giebeler, M. Herklotz, S. Oswald, J. Thomas, A. Meier, L. Borchardt, S. Kaskel, H. Ehrenberg and J. Eckert, *J. Mater. Chem. A*, 2013, **1**, 4904–4910.
- 12 X. L. Ji, K. T. Lee, R. Holden, L. Zhang, J. J. Zhang, G. A. Botton, M. Couillard and L. F. Nazar, *Nat. Chem.*, 2010, **2**, 286–293.
- 13 C. D. Liang, Z. J. Li and S. Dai, *Angew. Chem., Int. Ed.*, 2008, **47**, 3696–3717.
- 14 Y. Wan, Y. F. Shi and D. Y. Zhao, *Chem. Mater.*, 2008, **20**, 932–945.
- 15 M. Kruk, M. Jaroniec, R. Ryoo and S. H. Joo, *J. Phys. Chem. B*, 2000, **104**, 7960–7968.
- 16 B. Z. Fang, J. H. Kim, M. Kim and J. S. Yu, *Chem. Mater.*, 2009, **21**, 789–796.
- 17 T. Kyotani, L. F. Tsai and A. Tomita, *Chem. Mater.*, 1996, **8**, 2109–2113.
- 18 H. Q. Li, R. L. Liu, D. Y. Zhao and Y. Y. Xia, *Carbon*, 2007, **45**, 2628–2635.
- 19 Y. Lv, F. Zhang, Y. Dou, Y. Zhai, J. Wang, H. Liu, Y. Xia, B. Tu and D. Zhao, *J. Mater. Chem.*, 2012, **22**, 93–99.
- 20 J. Hu, M. Noked, E. Gillette, Z. Gui and S. B. Lee, *Carbon*, 2015, **93**, 903–914.
- 21 K. S. Xia, Q. M. Gao, J. H. Jiang and J. Hu, *Carbon*, 2008, **46**, 1718–1726.
- 22 K. P. S. Prasad, D. S. Dhawale, S. Joseph, C. Anand, M. A. Wahab, A. Mano, C. I. Sathish, V. V. Balasubramanian, T. Sivakumar and A. Vinu, *Microporous Mesoporous Mater.*, 2013, **172**, 77–86.
- 23 M. N. Patel, X. Q. Wang, D. A. Slanac, D. A. Ferrer, S. Dai, K. P. Johnston and K. J. Stevenson, *J. Mater. Chem.*, 2012, **22**, 3160–3169.
- 24 H. Li, J. Luo, X. Zhou, C. Yu and Y. Xia, *J. Electrochem. Soc.*, 2007, **154**, A731–A736.
- 25 D. W. Wang, F. Li, M. Liu, G. Q. Lu and H. M. Cheng, *J. Phys. Chem. C*, 2008, **112**, 9950–9955.
- 26 C. Z. Yang, C. Y. V. Li, F. J. Li and K. Y. Chan, *J. Electrochem. Soc.*, 2013, **160**, H271–H278.
- 27 F. J. Li, M. Morris and K. Y. Chan, *J. Mater. Chem.*, 2011, **21**, 8880–8886.
- 28 J. Duay, E. Gillette, J. K. Hu and S. B. Lee, *Phys. Chem. Chem. Phys.*, 2013, **15**, 7976–7993.
- 29 Z. Gui, J. Duay, J. Hu and S. B. Lee, *Phys. Chem. Chem. Phys.*, 2014, **16**, 12332–12340.
- 30 Z. D. Gao, X. Zhu, Y. H. Li, X. M. Zhou, Y. Y. Song and P. Schmuki, *Chem. Commun.*, 2015, **51**, 7614–7617.
- 31 J. Duay, S. A. Sherrill, Z. Gui, E. Gillette and S. B. Lee, *ACS Nano*, 2013, **7**, 1200–1214.
- 32 X. Zhao, C. Johnston and P. S. Grant, *J. Mater. Chem.*, 2009, **19**, 8755–8760.
- 33 J. B. Mu, B. Chen, Z. C. Guo, M. Y. Zhang, Z. Y. Zhang, P. Zhang, C. L. Shao and Y. C. Liu, *Nanoscale*, 2011, **3**, 5034–5040.
- 34 Q. H. Wang, L. F. Jiao, H. M. Du, Y. J. Wang and H. T. Yuan, *J. Power Sources*, 2014, **245**, 101–106.
- 35 Y. Meng, D. Gu, F. Q. Zhang, Y. F. Shi, H. F. Yang, Z. Li, C. Z. Yu, B. Tu and D. Y. Zhao, *Angew. Chem., Int. Ed.*, 2005, **44**, 7053–7059.
- 36 A. Corma, *Chem. Rev.*, 1997, **97**, 2373–2419.

- 37 Y. Meng, D. Gu, F. Q. Zhang, Y. F. Shi, L. Cheng, D. Feng, Z. X. Wu, Z. X. Chen, Y. Wan, A. Stein and D. Y. Zhao, *Chem. Mater.*, 2006, **18**, 4447–4464.
- 38 J. Jang and J. Bae, *Adv. Funct. Mater.*, 2005, **15**, 1877–1882.
- 39 M. R. Alexander, G. Beamson, P. Bailey, T. C. Q. Noakes, P. Skeldon and G. E. Thompson, *Surf. Interface Anal.*, 2003, **35**, 649–657.
- 40 M. B. Zheng, J. M. Cao, X. F. Ke, G. B. Ji, Y. P. Chen, K. Shen and J. Tao, *Carbon*, 2007, **45**, 1111–1113.
- 41 M. Zheng, G. Ji, Y. Wang, J. Cao, S. Feng, L. Liao, Q. Du, L. Zhang, Z. Ling, J. Liu, T. Yu, J. Cao and J. Tao, *Chem. Commun.*, 2009, 5033–5035.
- 42 T. W. Kim and L. A. Solovyov, *J. Mater. Chem.*, 2006, **16**, 1445–1455.
- 43 S. A. Chambers, Y. J. Kim and Y. Gao, *Surf. Sci. Spectra*, 1998, **5**, 219–228.
- 44 H. C. Chen, C. C. Wang and S. Y. Lu, *J. Mater. Chem. A*, 2014, **2**, 16955–16962.
- 45 S. Y. Wang, K. C. Ho, S. L. Kuo and N. L. Wu, *J. Electrochem. Soc.*, 2006, **153**, A75–A80.
- 46 X. Zhao, C. Johnston, A. Crossley and P. S. Grant, *J. Mater. Chem.*, 2010, **20**, 7637–7644.
- 47 L. Wang, H. M. Ji, S. S. Wang, L. J. Kong, X. F. Jiang and G. Yang, *Nanoscale*, 2013, **5**, 3793–3799.
- 48 D. Liu, X. Wang, X. Wang, W. Tian, J. Liu, C. Zhi, D. He, Y. Bando and D. Golberg, *J. Mater. Chem. A*, 2013, **1**, 1952–1955.
- 49 N. L. Wu, S. Y. Wang, C. Y. Han, D. S. Wu and L. R. Shiue, *J. Power Sources*, 2003, **113**, 173–178.
- 50 E. Barsoukov and J. R. Macdonald, *Impedance spectroscopy: theory, experiment, and applications*, John Wiley, Hoboken, N.J., 2nd edn, 2005.
- 51 A. J. Bard and L. R. Faulkner, *Electrochemical methods: fundamentals and applications*, John Wiley, New York, 2nd edn, 2001.
- 52 M. Patel, X. Wang, D. Slanac, D. Ferrer, S. Dai, K. Johnston and K. Stevenson, *J. Mater. Chem.*, 2012, **22**, 3160–3169.
- 53 M. W. Xu, W. Jia, S. J. Bao, Z. Su and B. Dong, *Electrochim. Acta*, 2010, **55**, 5117–5122.
- 54 X. Du, C. Wang, M. Chen, Y. Jiao and J. Wang, *J. Phys. Chem. C*, 2009, **113**, 2643–2646.
- 55 R. Z. Li, X. Ren, F. Zhang, C. Du and J. P. Liu, *Chem. Commun.*, 2012, **48**, 5010–5012.
- 56 M. E. Orazem and B. Tribollet, *Electrochemical impedance spectroscopy*, Wiley, Hoboken, N.J., 2008.
- 57 J. C. Wang, *J. Electrochem. Soc.*, 1987, **134**, 1915–1920.
- 58 M. Sluytersrehabach, *Pure Appl. Chem.*, 1994, **66**, 1831–1891.
- 59 J. Bisquert, *Phys. Chem. Chem. Phys.*, 2000, **2**, 4185–4192.